Modeling Dielectric-constant values of Geologic Materials: An Aid to Ground-Penetrating Radar Data Collection and Interpretation

Alex Martinez* and Alan P. Byrnes
Kansas Geological Survey, 1930 Constant Avenue, Lawrence, KS 66047

*Current Position: ExxonMobil Exploration Company, P.O. Box 4778, Houston, TX 77210-4778

Abstract

Ground-penetrating radar (GPR) is a near-surface geophysical imaging technique used for non-intrusive subsurface geologic and engineering investigations. Dielectric constant is a critical parameter for GPR surveys because it controls propagation velocity of electromagnetic waves through material, reflection coefficients across interfaces of different materials, and vertical and horizontal imaging resolution. Dielectric constant in rocks and sediments is primarily a function of mineralogy, porosity, pore fluids, frequency, geometries, and electrochemical interactions between rock components. Reported dielectric-constant values for sedimentary rocks provide general ranges of expected values, but these values may not adequately represent rocks in specific field conditions.

Time-propagation mixing modeling, a forward-modeling technique, was performed and showed good correlation between modeled and measured dielectric constants of selected sandstones and limestones. Additional models were constructed to investigate the role of lithology and fluid saturation on dielectric constant and GPR response.

Three modeled rock examples of variable mineralogy, porosity, and saturation illustrate that bulk dielectric constant, which generally ranges from 2 to 38 in the materials modeled, is primarily controlled by water saturation and, secondarily, by porosity and mineralogy, although these variables are interdependent. Without data stacking, differences in dielectric constant must be greater than 2 to produce reflections that can be recorded above background noise. For the examples modeled, saturation differences of less than 35% between layers produced reflection signals above background noise, but in completely dry material, normal mineralogic and porosity differences may not produce discernible reflections without stacking.

Introduction

Ground-penetrating radar (GPR) is a geophysical technique, similar to seismic reflection, that uses electromagnetic (EM), rather than acoustic, waves to image the shallow subsurface (Ulriksen, 1982; Davis and Annan, 1989; Daniels, 1996). GPR has been used to aid in geologic (e.g., Pratt and Miall, 1993; Liner and Liner, 1995; McMechan et al., 1998), hydrologic (e.g., Annan et al., 1991; Knoll and Clement, 1999), engineering (e.g., Botelho et al., 1998), archeological (e.g., Dolphin et al., 1978), and petroleum (Knight and Endres, 1990) investigations.

GPR operates in the electrical conduction wavelength region of the electromagnetic spectrum. Whereas seismic response is a function of acoustic properties, GPR response is a function of the electromagnetic properties: dielectric permittivity (*e*), magnetic permeability (*m*), and electrical conductivity (*s*). Dielectric permittivity is a complex function having real and imaginary components. The real portion of dielectric permittivity is usually expressed as dielectric constant (e_r), which is the ratio of the electric-field storage capacity of a material to that of free space. The imaginary portion of dielectric permittivity is usually expressed as dielectric loss, which represents attenuation and dispersion. Dielectric loss is negligible if the conductivity of a material is low, less than ~10 milliSiemens/meter (mS/m), as it is for many geologic materials. Thus, dielectric constant is typically the primary component of dielectric permittivity. Magnetic permeability, the magnetic field divided by the magnetic field strength, is the product of the permeability of free space (m_0) and relative magnetic permeability (m_r). The effect of magnetic permeability on GPR response is negligible for materials with a relative magnetic permeability value of $m_r = 1$, which is the value for most sedimentary materials. Dielectric permittivity, magnetic permeability, and electric conductivity are frequency dependent and behave differently over various frequency ranges (Powers, 1997). Dielectric constant generally decreases with increasing frequency, while conductivity and dielectric loss increase with increasing frequency. However, their behavior is relatively consistent over the typical GPR antenna frequency range of 25–1,500 MHz.

Dielectric constant is a critical GPR parameter because it controls the propagation velocity of electromagnetic waves through a material and the reflection coefficients at interfaces, as well as affecting the vertical and horizontal imaging resolution. Therefore, knowing dielectric-constant values of materials helps in planning GPR surveys and in better understanding and interpreting GPR images.

Measured dielectric-constant values for various rocks and minerals may be found in the literature (e.g., Davis and Annan, 1989; Daniels, 1996; Olhoeft, 1989; Schon, 1996; Ulaby et al., 1990). Reported bulk dielectric-constant values of common earth materials are presented in table 1, and reported dielectric-constant values of common minerals and fluids are presented in table 2. These data are broadly useful; however, bulk dielectric constants of rocks and sediments actually reflect complex mixtures of materials and architectures that vary from one rock lithology to the next. In rocks and sediments, dielectric properties are primarily a function of mineralogy, porosity, water saturation, frequency, and depending on the rock lithology, component geometries, and electrochemical interactions (Knight and Endres, 1990; Knoll, 1996). Variations in each of these parameters can significantly change bulk dielectric constants. Dielectric mixing modeling is a forward-modeling technique that provides a basis for predicting expected bulk dielectric-constant values based on specific input parameters. Numerous dielectric-constant mixing models have been proposed, and all fall within four broad categories: effective medium, empirical and semi-empirical, phenomenological, and volumetric (Knoll, 1996) (table 3).

TABLE 1. Bulk dielectric constants (ε_r measured at 100 MHz) of common earth materials.

Material	ε_r (Davis and Annan, 1989)	ε_r (Daniels , 1996)
Air	1	1
Distilled water	80	
Fresh water	80	81
Sea water	80	
Fresh water ice	3–4	4
Sea water ice		4–8
Snow		8–12
Permafrost		4–8
Sand, dry	3–5	4–6
Sand, wet	20–30	10–30
Sandstone, dry		2–3
Sandstone, wet		5–10
Limestone	4–8	
Limestone, dry		7
Limestone wet		8
Shales	5–15	
Shale, wet		6–9
Silts	5–30	
Clays	5–40	
Clay, dry		2–6
Clay, wet		15–40
Soil, sandy dry		4–6
Soil, sandy wet		15–30
Soil, loamy dry		4–6
Soil, loamy wet		10–20
Soil, clayey dry		4–6
Soil, clayey wet		10–15
Coal, dry		3.5
Coal, wet		8
Granite	4–6	
Granite, dry		5
Granite, wet		7
Salt, dry	5–6	4–7

This paper provides a brief discussion of dielectric-constant mixing models, a general review of the important equations governing GPR response, and presents an application of Time-Propagation (TP) dielectric mixing modeling to predict reflection coefficients, reflection travel-times, and imaging resolution. Three examples illustrate TP modeling of sandstones and carbonates, and the relationship between dielectric constant and porosity (ϕ), mineralogy (X_m), water saturation (S_w), fluid-rock electrochemical interaction, and hydraulic permeability (k). A downloadable Excel 97 workbook containing interactive worksheets involving TP modeling and reflection coefficient and two-way travel time modeling is included as appendix A (http://www.kgs.ukans.edu/Current/2001/martinez/Appendix_A.xls).

Basic Aspects of the TP Mixing Model

Numerous dielectric-constant mixing models have been proposed in the literature, and all fall within the four general categories shown in table 3. Each type of model has inherent strengths and weaknesses based on the assumptions intrinsic to the model. Some model types (e.g., effective medium and phenomenological) work well with relatively homogeneous materials such as ice, but are less effective for more complex, heterogeneous materials. Other model types (e.g., empirical and semi-empirical) can accurately predict values for the data used to construct them, but are not widely applicable to data sets consisting of different mineralogies, porosities, or water saturations. An excellent summary of dielectric mixing models can be found in Knoll (1996).

The dielectric mixing model found by the authors to be the most useful and easiest to implement for geologic materials is the Time-Propagation (TP) model, a volumetric model. Not only are the input parameters easily obtained, but the mathematical equation to calculate bulk dielectric-constant values is simple (and therefore widely usable) and the results of the TP model are very similar to observed values. The mathematical equation describing the TP dielectric mixing model is:

$$\varepsilon_r = [\Sigma V_i (\varepsilon_{ri})^{0.5}]^2, \quad (1)$$

where V_i and ε_{ri} are the bulk volume fraction and dielectric constant, respectively, of the ith component (Knoll, 1996). Equation (1) is a specific instance of the more general Lichtenecker-Rother equation (Lichtenecker and Rother, 1931):

$$\varepsilon = [\Sigma V_i (\varepsilon_i)^{\alpha}]^{1/\alpha}, \quad (2)$$

where α, a geometric factor that relates the direction of the

TABLE 2. Dielectric constants of common minerals and fluids. Note: These values are for specific minerals and fluids from specific study sites. Minerals and fluids taken from other sites may have slightly different dielectric constant values or may exhibit dielectric anisotropy.

Material	Dielectric Constant	Frequency (MHz)	Source
Acetone	20.9	1	Lucius et al., 1989
Albite	7.0	1	Olhoeft, 1989
Air	1.0	1	Lucius et al., 1989
Benzene	2.3	1	Lucius et al., 1989
Calcite	6.4	1	Olhoeft, 1989
Calcite	7.8–8.5	Radio	Keller, 1989
Carbon tetrachloride	2.2	1	Lucius et al., 1989
Chloroform	4.8	1	Lucius et al., 1989
Cyclohexane	2.0	1	Lucius et al., 1989
Ethylene glycol	38.7	1	Lucius et al., 1989
Gypsum	6.5	750	Martinez and Byrnes, 1999
Halite	5.9	1	Olhoeft, 1989
Ice	3.4	1	Olhoeft, 1989
Kaolinite	11.8	1	Olhoeft, 1989
Methanol	33.6	1	Lucius et al., 1989
Mica	6.4	750	Martinez and Byrnes, 1999
Montmorillonite	210	1	Olhoeft, 1989
Olivine	7.2	1	Olhoeft, 1989
Orthoclase	5.6	1	Olhoeft, 1989
Pyroxene	8.5	1	Olhoeft, 1989
Quartz	4.5	1	Olhoeft, 1989
Tetrachloroethene	2.3	1	Lucius et al., 1989
Trichloroethene	3.4	1	Lucius et al., 1989
Water	80	1	Lucius et al., 1989

TABLE 3. Summary of dielectric mixing model categories (adapted from Knoll, 1996).

Effective medium
Method: Computes dielectric properties by successive substitutions
Types: Bruggeman-Hanai-Sen (BHS)
Advantages: Accurate for known geometries
Disadvantages: Cumbersome to implement; need to choose number of components, initial material, and order and shape of replacement material
References: Sen et al., 1981; Ulaby et al., 1986

Empirical and semi-empirical
Method: Mathematical functional relationship between dielectric and other measurable properties
Types: Logarithmic; Polynomial
Advantages: Easy to develop quantitative relationships; able to handle complex materials in models
Disadvantages: There may be no physical justification for the relationship; valid only for the specific data used to develop the relationship and may not be applicable to other data sets
References: Dobson et al., 1985; Olhoeft and Strangway, 1975; Topp et al., 1980; Wang and Schmugge, 1980

Phenomenological
Method: Relates frequency dependent behavior to characteristic relaxation times
Types: Cole-Cole; Debye
Advantages: Does not need component properties or geometrical relationships
Disadvantages: Dependent on frequency-specific parameters
References: Powers, 1997; Ulaby et al., 1986; Wang, 1980

Volumetric
Method: Relates bulk dielectric properties of a mixture to the dielectric properties of its constituents
Types: Complex Refractive Index (CRIM); Arithmetic average; Harmonic average; Lichetenecker-Rother; Time-Propagation (TP)
Advantages: Volumetric data relatively easy to obtain
Disadvantages: Does not account for micro-geometry of components; does not account for electrochemical interaction between components
References: Alharthi and Lange, 1987; Birchak et al., 1974; Knoll, 1996; Lange, 1983; Lichtenecker and Rother, 1931; Roth et al., 1990; Wharton et al., 1980

effective layering of components to the direction of the applied electrical field, is 0.5 (Knoll, 1996). The TP model does not account for variations in frequency; therefore, modeled bulk dielectric-constant values are valid only at the specific frequency for which the input component dielectric constants are representative. This model also does not account for the effects of dielectric loss or magnetic permeability; therefore, it is valid only for predicting the dielectric constant of low-loss (i.e., low conductivity; $\sigma < 10$ mS/m), nonmagnetic (i.e., $\mu_r \approx 1$) materials.

Because at a given frequency there are three principal variables (mineralogy, porosity, and water saturation) exerting control on bulk dielectric-constant values in low-loss rocks and soils, it is possible to represent the TP model results in four-dimensions (termed TP-model dielectric-constant space on fig. 1). For most rocks and soils, porosity ranges from 0% to 50% (expressed as percent of total rock volume) and water saturation ranges from 0% to 100% (expressed as percentage of pore volume). It is convenient to express mineralogy in units of the dielectric constant of the mineral mixture at zero porosity and water saturation. On this basis, the influence of mineralogy for most common rocks and soils ranges from a low value exhibited by quartz ($X_m \sim 4$) to a high value exhibited by kaolinite ($X_m \sim 12$).

Many GPR investigations are conducted in the vadose zone where water saturations can vary with the capillary-pressure properties of the rock or soil. Figure 2A shows

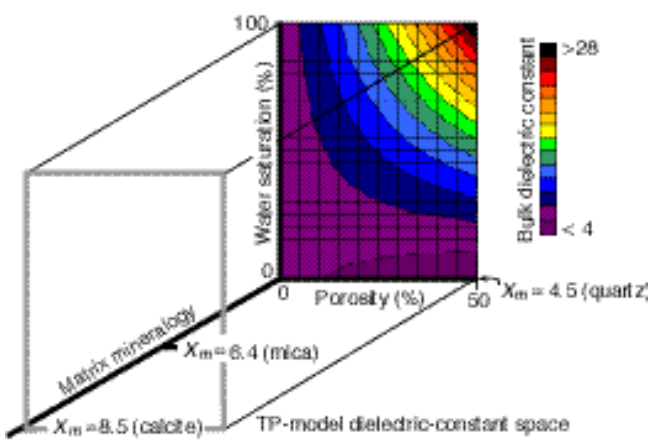

FIGURE 1. Four-dimensional representation (termed TP-model dielectric-constant space) of the TP-model input parameters (matrix mineralogy, porosity, and water saturation) and resulting bulk dielectric constant values (shown in color). The matrix mineralogy axis (X_m) is the dielectric-constant value of the matrix components at zero porosity and water saturation. The locations of quartz, mica, and calcite are indicated on the X_m axis. For most earth materials, porosity ranges from 0% to 50%, and water saturation ranges from 0% to 100%. Calculated bulk dielectric-constant values range from greater than 4 to less than 28. The N-S_w planes through $X_m = 4.5$ (quartz) and $X_m = 8.5$ (calcite) are shown in fig. 2.

the relationship between bulk dielectric constant and both porosity and water saturation for a quartz matrix ($X_m = 4.5$). At water saturations below approximately 20%, which can be common in the vadose zone for many higher porosity rocks and soils, bulk dielectric constant remains below 6.0 for porosities ranging from zero to 50%. Even for rocks with minerals exhibiting relatively high dielectric-constant values (e.g., calcite, $\varepsilon_r = 8.5$), the bulk dielectric constant is less than 8.0 (fig. 2B). These low bulk dielectric-constant values are mainly the result of the low dielectric constant of the minerals and the low dielectric constant of air ($\varepsilon_r = 1.0$) occupying the pore space. As water saturation increases, the higher dielectric constant of water ($\varepsilon_r = 81$) increases bulk dielectric-constant values to greater than 30 (fig. 2). Worksheets 2 and 3 (appendix A) allow construction of figures similar to fig. 2 for user-defined porosity, mineralogy, and water saturation.

Dielectric Constant and Ground-Penetrating Radar

The results of dielectric-constant modeling can be used in planning GPR data acquisition and in interpreting GPR data. For data acquisition, modeling results can be used to determine whether a feature or interface will result in measurable reflections, and if so, the expected two-way reflection travel-times (*TWT*) and antenna frequencies needed for imaging. For interpretation, dielectric-modeling results can be used to better understand recorded travel-times and amplitude variations, the controlling factors on measured dielectric property values. These results are also necessary for inverse modeling sediment or rock properties from GPR response. A review of the equations governing GPR response illustrates the role of dielectric constant.

All equations presented below assume that reflections are at or near vertical incidence and that the material through which the EM waves travel is of low conductivity ($\sigma < 10$ mS/m) and nonmagnetic ($\mu_r = 1$). (When reflections are not at vertical incidence, the more general relationships presented in Baker, 1998, and Reppart et al., 1999, become more valid mathematical representations of the electromagnetic wave-field response.) The assumptions of low-conductivity and nonmagnetic material are valid for most nonclayey, sedimentary materials containing freshwater in their pore spaces. The results of the equations become less valid as conditions vary from the initial assumptions (i.e., $\sigma > 10$ mS/m and $\mu_r \neq 1$) due to the dispersive effect of conductivity and the added influence of relative magnetic permeability on wave propagation.

Reflection Coefficients and Power Reflectivity

The reflection coefficient (*RC*) of GPR signals in nonmagnetic material is a function of electromagnetic impedance (EM). If EM is replaced with its equivalent,

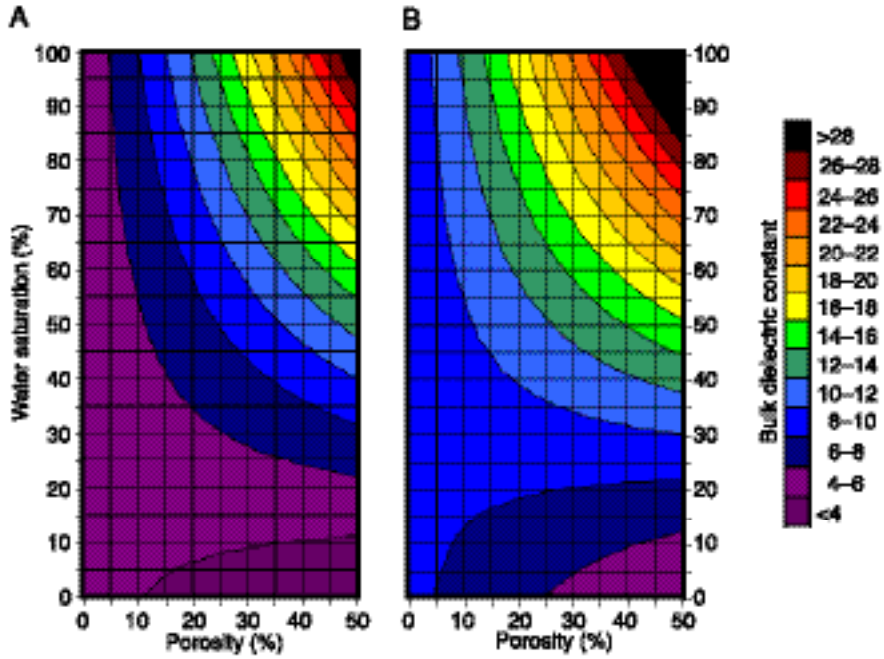

FIGURE 2. TP-modeled bulk dielectric constants for (A) X_m = 4.5 (quartz) and (B) X_m = 8.5 (calcite), with porosities ranging from 0% to 50% and water saturations ranging from 0% to 100%. At low water saturations, bulk dielectric-constant values decrease slowly with increasing porosity due to the increased influence of air (ε_r = 1), which has a dielectric constant near that of common earth materials (ε_r ~ 4–12). At high water saturations, bulk dielectric-constant values increase rapidly with increasing porosity due to the increased influence of the high dielectric constant of water (ε_r = 81).

the square root of the dielectric constant, the reflection coefficient can be calculated:

$$RC = [(\varepsilon_{r1})^{1/2} - (\varepsilon_{r2})^{1/2}] / [(\varepsilon_{r1})^{1/2} + (\varepsilon_{r2})^{1/2}], \quad (3)$$

where ε_{r1} is the dielectric constant of the upper media and ε_{r2} is the dielectric constant of the lower media. Equation (3) can be used to determine the strength of reflections at interfaces of materials of different lithology or water saturations (i.e., different bulk dielectric constants). Worksheet 4 (appendix A) can be used to calculate the change in reflection coefficient as the result of dielectric-constant change between materials.

Power reflectivity (P_r) is a measure of the energy reflected by a target back to a receiving antenna. If the power reflectivity is too low compared to background clutter (noise), then a reflection may not be recorded by a GPR system—in other words, the signal-to-noise ratio (SNR) is below 1. The power reflectivity (P_r) of an interface may be estimated using the relationship presented by Annan (1996):

$$P_r = (RC)^2. \quad (4)$$

A conservative guideline is that power reflectivity should be greater than 0.01 or that *RC* should exceed 0.10 (Annan, 1996) in order for GPR to discern a reflection above background noise for single-fold data. The power reflectivity increases for GPR data when vertical and CMP stacking (the summing of traces) are employed to increase fold in low-loss, low-EM noise regions. The power reflectivity decreases for targets with diameters less than the EM wavelength or in regions with high loss and high EM noise. Annan's (1996) reflection-coefficient threshold of 0.10 is only a general guideline, but it provides a useful frame of reference. The SNR of a reflection increases as a function of the square root of the number of stacks (Yilmaz and Doherty, 1987); therefore, stacking may allow low power reflectivity reflections to be recorded (fig. 3). Unlike seismic data, where stacking requires considerably greater effort, obtaining 64 or 128 vertical stacks of a GPR trace may only take several seconds longer than a single-fold trace.

Velocity and Travel-time

The velocity (*V*) at which electromagnetic waves travel through low-loss materials is described by the relationship:

$$V = c / (\varepsilon_{r\text{-}bulk})^{0.5}, \quad (5)$$

where *c* is the speed of light in a vacuum (3×10^8 m/s). Because dielectric-constant values of rock exceed the dielectric constant of a vacuum (ε_r = 1), electromagnetic velocity is greatest in a vacuum and decreases with increasing dielectric constant. Velocity information can be used to calculate expected two-way travel-times (*TWT*) of reflections using the relationship:

$$TWT = 2d / V, \quad (6)$$

where *d* is distance to the reflector. Travel-times determine the optimal data recording time-window for a GPR survey and are essential to the interpretation of GPR data.

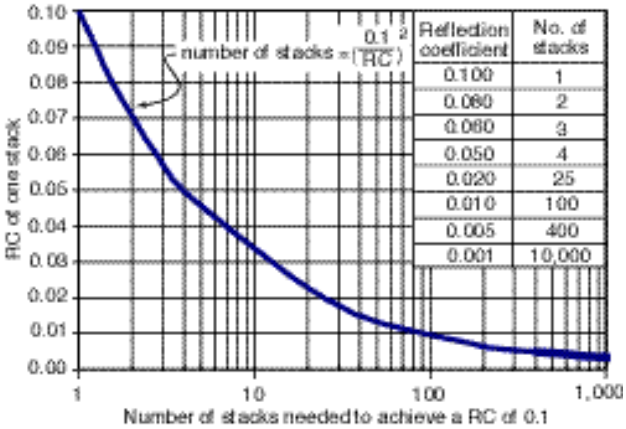

FIGURE 3. Plot of the reflection coefficient of single-fold data versus the number of stacks needed to achieve a reflection coefficient of 0.1, the minimum threshold value established by Annan (1996), in which the signal-to-noise (SNR) ratio is approximately 1. The values are calculated using the assumption that stacking increases the SNR by a factor of the square root of the number of stacks, which is true for random noise (Yilmaz and Doherty, 1987).

Travel-times provide expected reflection times for reflectors at given depths and predict the maximum depth of meaningful GPR penetration.

Vertical and Spatial Resolution

Maximum vertical imaging resolution is usually considered to be one-quarter of the predominant wavelength ($\lambda_{1/4}$) (Yilmaz and Doherty, 1987):

$$\lambda_{1/4} = V / (4f), \tag{7}$$

where f is frequency. Equation (7) was used to construct fig. 4, which shows the optimal vertical resolution for dipole antennas with a bandwidth equal to 1 ± 0.5 of the center frequency (e.g., f = 225–675 MHz for a 450-MHz antenna), a common GPR antenna design.

Spatial resolution is determined by the area of the region illuminated by a GPR antenna, often referred to as the Fresnel zone or antenna footprint. For bistatic dipole antennas, the area of the antenna footprint can be approximated using the relationships:

$$A = \lambda_{1/4} + [z(0) - z(d)]/(\varepsilon_r - 1)^{1/2} \tag{8}$$

and

$$B = A/2, \tag{9}$$

where A is the radius of the Fresnel zone parallel to the long axis at depth $z(d)$, B is the radius perpendicular to the long axis at depth $z(d)$, $z(d)$ is the depth of the Fresnel zone in the subsurface, and $z(0)$ is the antenna elevation relative to ground level (Annan, 1996) (fig. 5). Equations (8) and (9) and fig. 5 indicate that GPR patterns become more focused with increasing dielectric constant, resulting in greater spatial resolution. The equations can be used to determine antenna frequencies suitable for imaging subsurface targets with known spatial dimensions.

Application of Dielectric Mixing Modeling

Example 1: Theoretical TP modeling of bulk dielectric constant in sandstones

Because of the high dielectric constant of freshwater (ε_r = 81), the water saturation of a material can greatly affect bulk dielectric-constant values. To gain a better understanding of the effects of water saturation in sandstones, the TP model was used to generate bulk dielectric constant, two-way travel-time, and reflection-coefficient values for three common field scenarios involving two layers of differing lithology, porosity, and water saturation. Models were constructed with varying amounts of quartz (ε_r = 4.5), mica (ε_r = 6.4), air (ε_r = 1), and water (ε_r = 81), and are presented in order of increasing complexity. Modeling results are summarized in table 4. As noted earlier, the TP model is valid only in low-loss materials, where there is no attenuation due to conductivity from clay-induced cation-exchange-capacity (CEC). These results can be used to provide expected reflection coefficient and travel-time values for a range of water saturations.

Scenario 1—Effect of Water Saturation on a Homogeneous Sandstone

This model simulates the effect of a water table on reflection coefficient and two-way travel-times for a 1-m-thick, lithologically homogeneous (100% quartz) sandstone with 35% porosity. Water saturation in the upper 0.5

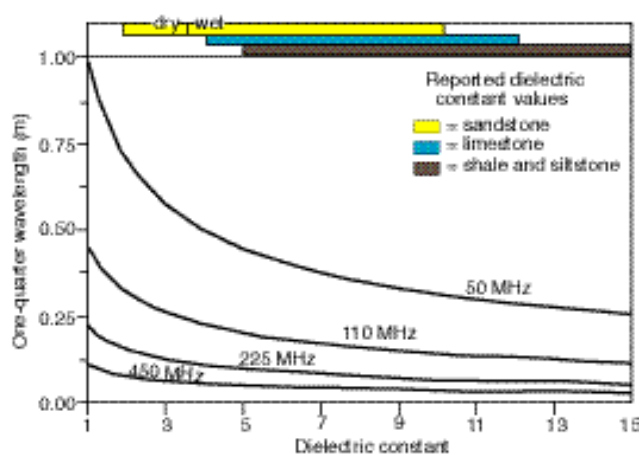

FIGURE 4. Plot of dielectric constant versus maximum vertical imaging resolution for bistatic, dipole antennas with a bandwidth equal to 1 ± 0.5 of their center frequency. Typical dielectric constant ranges for sedimentary rocks are shown as bars. The dielectric constant values are a summary of values given in Annan (1996), Daniels (1996), and Schon (1996).

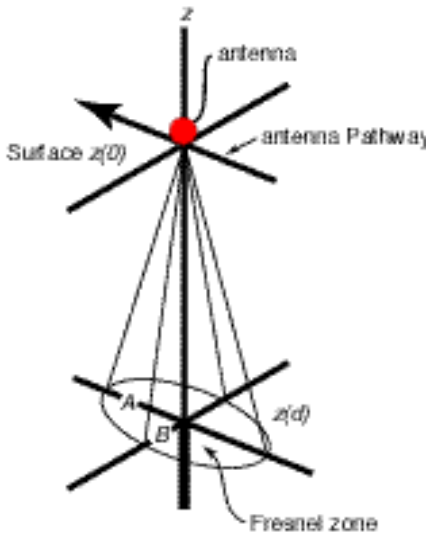

Figure 5. Approximate GPR-antenna footprint (Fresnel zone) for bistatic, dipole antennas (adapted from Annan, 1996). This footprint is calculated using Equations (8) and (9). *A* = long radius; *B* = short radius; *z* = elevation, where *z(0)* is the surface elevation and *z(d)* is the depth of the Fresnel zone.

m was assigned a constant value of 10% (near irreducible water saturation), and water-saturation values in the lower 0.5 m were sequentially increased from 10% to 100% and then decreased back down to 10%.

The results of this model are summarized in section 1 of table 4 and are shown in time-lapse sequence in fig. 6A (fig. 6A can be viewed at http://www.kgs.ukans.edu/Current/2001/martinez/fig6A.html). For a water saturation of 10% in both layers, the two-way travel-time for the entire interval is 13.39 ns and the reflection coefficient is zero (there is no impedance contrast). As fig. 6A illustrates, increasing water saturation in the lower sandstone interval (shown as an increasing blue bar on the water saturation column on the left) results in increased bulk dielectric-constant values in the lower layer (central column), increased two-way travel-time for the entire interval (right column), and increased reflection-coefficient values for the interface (horizontal black bar in right column). For increasing lower-layer water saturations, the two-way travel times for the entire interval increase and reflection coefficients increase in magnitude (fig. 6B). These data indicate that, without stacking, saturation differences between the layers must exceed 15% to produce a reflection coefficient that is above background noise (*RC* greater than 0.10). Based on Eq. (4), obtaining nine vertical stacks would increase the reflection coefficient to 0.1 (for a 5% difference in water saturation). For single-stack data, with decreasing porosity, the consequent decreased volume of water in the bulk volume requires greater saturation differences between the layers to produce a reflection coefficient above 0.10. Calculations using worksheet 5 (appendix A) indicate that differences in saturation must exceed 35% at 15% porosity; at 5% porosity, even total saturation of the lower layer (S_w = 100%) will not generate sufficient contrast in dielectric-constant values between the layers to produce a reflection coefficient greater than 0.10.

Scenario 2—Effect of Water Saturation on a Sandstone with Porosity Variations

In this scenario, variations in porosity were simulated that are characteristic of some fluvial sandstone deposits (in which coarse-grained, more porous sands may overlie finer-grained, less porous sands or where there is a coarsening-upward sequence). The upper 0.5-m-thick sandstone layer consists of 100% quartz with 35% porosity and the lower 0.5-m-thick sandstone layer is 100% quartz with 20% porosity. Throughout the simulation, water saturation in both layers was equal, ranging from 0% to 100%.

Modeling results are summarized in section 2 of table 4 and are shown in time-sequence in fig. 7A (fig. 7A can be viewed at http://www.kgs.ukans.edu/Current/2001/martinez/fig7A.html). Total interval two-way travel-times for this model increase from 12.09 ns at 0% water saturation to 26.75 ns at 100% water saturation. Increasing the water saturation of both layers by the same relative percentage of the available porosity produced low reflection-coefficient values that approach a minimum between 10% and 15% water saturation. At 15% water saturation in both layers, the reflection coefficient reverses polarity and reaches a maximum value of 0.13 at 100% water saturation (fig. 7B). The minimum in this series of models reflects the difference in bulk volume water ($BVW = \phi S_w$; porosity times saturation) between the layers, although

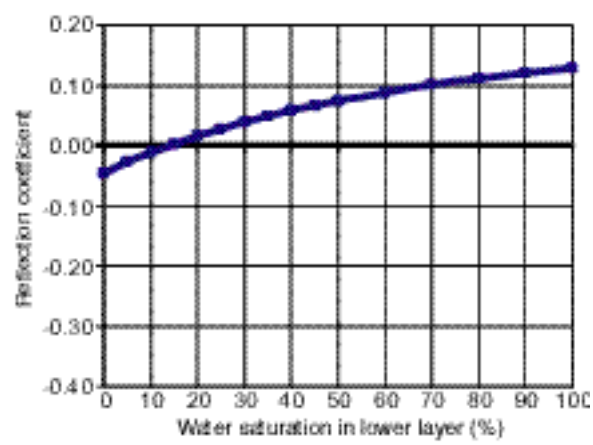

Figure 6B. Reflection coefficient at the interface between upper and lower layers versus water saturation of the lower layer in a 1-m (3.3-ft)-thick, 35% porosity, 100% quartz sandstone with a fixed water saturation of 10% in the upper 0.5 m (1.6 ft) and variable water saturation (10% to 100%) in the lower 0.5 m (1.6 ft). **Note: fig. 6A can be viewed at http://www.kgs.ukans.edu/Current/2001/martinez/fig6A.html.**

TABLE 4. Dielectric modeling results of the effect of water saturation on sandstones. Gray shading indicates $P_r < 0.01$, a situation where reflection values may be difficult to record in high-noise field conditions.

Model	Upper : Lower Water Saturation (%)	Bulk Dielectric Constant upper layer	Bulk Dielectric Constant lower layer	Reflection Coefficient	TWT to Interface (ns)	TWT for Entire Interval (ns)
1: Homogeneous sandstone (fig. 6A,B)	10:10	4.04	4.04	0	6.70	13.39
	10:15	4.04	4.62	-0.0337	6.70	13.86
	10:20	4.04	5.24	-0.0651	6.70	14.33
	10:25	4.04	5.90	-0.0946	6.70	14.79
	10:30	4.04	6.60	-0.1223	6.70	15.26
	10:35	4.04	7.34	-0.1484	6.70	15.73
	10:40	4.04	8.12	-0.1729	6.70	16.19
	10:45	4.04	8.93	-0.1961	6.70	16.66
	10:50	4.04	9.79	-0.2180	6.70	17.13
	10:55	4.04	10.69	-0.2387	6.70	17.59
	10:60	4.04	11.62	-0.2584	6.70	18.06
	10:65	4.04	12.59	-0.2771	6.70	18.53
	10:70	4.04	13.61	-0.2949	6.70	18.99
	10:80	4.04	15.75	-0.3279	6.70	19.93
	10:90	4.04	18.05	-0.3580	6.70	20.86
	10:100	4.04	20.51	-0.3855	6.70	21.79
2: Sandstone with variable porosity (fig. 7A, B)	0:0	2.99	3.60	-0.0464	5.76	12.09
	5:5	3.49	3.91	-0.0281	6.23	12.82
	10:10	4.04	4.23	-0.0119	6.70	13.55
	15:15	4.62	4.57	0.0028	7.16	14.29
	20:20	5.24	4.92	0.0159	7.63	15.02
	25:25	5.90	5.28	0.0279	8.10	15.75
	30:30	6.60	5.65	0.0388	8.56	16.49
	35:35	7.34	6.04	0.0487	9.03	17.22
	40:40	8.12	6.44	0.0579	9.50	17.95
	45:45	8.93	6.85	0.0663	9.96	18.69
	50:50	9.79	7.27	0.0741	10.43	19.42
	60:60	11.62	8.16	0.0881	11.36	20.89
	70:70	13.61	9.10	0.1002	12.30	22.35
	80:80	15.75	10.09	0.1108	13.23	23.82
	90:90	18.05	11.14	0.1202	14.16	25.29
	100:100	20.51	12.23	0.1286	15.10	26.75
3: Sandstone with variable lithology and porosity (fig. 8A,B)	0:0	2.99	4.10	-0.0791	5.76	12.52
	5:5	3.49	4.43	-0.0596	6.23	13.25
	10:10	4.04	4.78	-0.0422	6.70	13.98
	15:15	4.62	5.13	-0.0265	7.16	14.72
	20:20	5.24	5.50	-0.0123	7.63	15.45
	25:25	5.90	5.88	0.0006	8.10	16.18
	30:30	6.60	6.28	0.0124	8.56	16.92
	35:35	7.34	6.69	0.0232	9.03	17.65
	40:40	8.12	7.11	0.0332	9.50	18.38
	45:45	8.93	7.54	0.0424	9.96	19.12
	50:50	9.79	7.99	0.0509	10.43	19.85
	60:60	11.62	8.92	0.0661	11.36	21.32
	70:70	13.61	9.90	0.0794	12.30	22.78
	80:80	15.75	10.93	0.0911	13.23	24.25
	90:90	18.05	12.01	0.1015	14.16	25.72
	100:100	20.51	13.15	0.1107	15.10	27.18

percent water saturation is constant for both layers. Reflection coefficients for these models do not exceed 0.10 except at water saturations greater than 70%, indicating that no significant reflection would occur at the interface between these layers without data stacking. Though not simulated in fig. 7A, most sandstones would be expected to have higher water saturations in the lower layer than in the upper layer due to pore-size-induced differences in capillary pressure. Calculations using worksheet 5 (appendix A) for this model indicate that single-stack reflection-coefficient values exceed 0.10 only at water saturations greater than 35% in the lower layer.

Scenario 3—Effect of Water Saturation on a Heterogeneous Sandstone

This model was constructed to simulate variations in porosity and lithology. The model consists of an upper 0.5-m-thick sandstone layer of 100% quartz with 35% porosity and a lower 0.5-m-thick silty sandstone layer of 60% quartz and 40% mica with 20% porosity.

Modeling results are summarized in section 3 of table 4 and are shown in time-sequence in fig. 8A (fig. 8A can be viewed at http://www.kgs.ukans.edu/Current/2001/martinez/fig8A.html). When water saturation in both

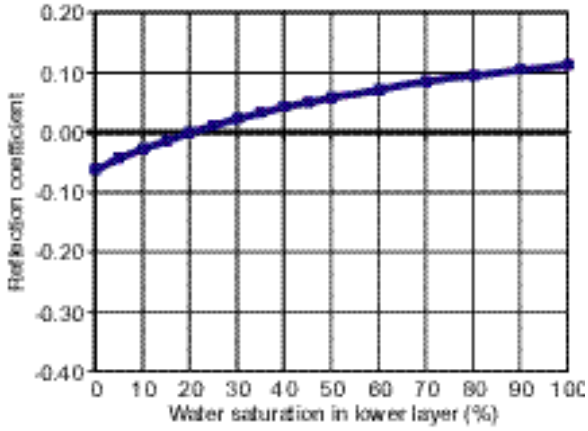

FIGURE 7B. Reflection coefficient at the interface between upper and lower layers versus water saturation of the lower layer in a 1-m (3.3-ft)-thick, 35% porosity, 100% quartz sandstone with a fixed water saturation of 10% in the upper 0.5 m (1.6 ft) and variable water saturation (10% to 100%) in the lower 0.5 m (1.6 ft). **Note: fig. 7A can be viewed at http://www.kgs.ukans.edu/Current/2001/martinez/fig7A.html.**

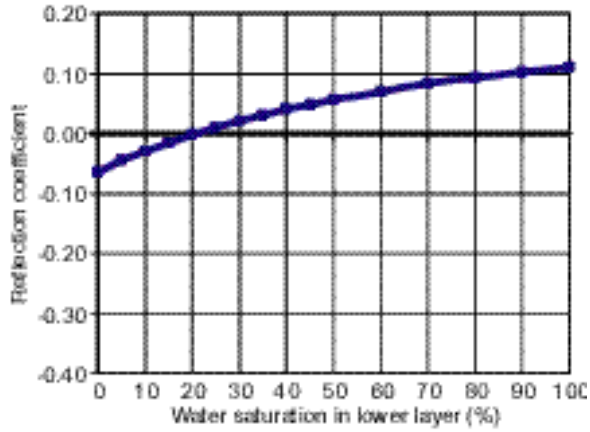

Fig. 8B. Reflection coefficient at interface between upper and lower layers versus water saturation present in both layers in a 0.5-m (1.6-ft)-thick, 35% porosity, 100% quartz layer overlying a 0.5-m (1.6-ft)-thick, 20% porosity, 60% quartz, 40% mica layer. **Note: fig. 8A can be viewed at http://www.kgs.ukans.edu/Current/2001/martinez/fig8A.html.**

layers is 0%, *TWT* values are 12.52 ns; these values increased to 27.18 ns at 100%, an increase similar to that seen in the two previous scenarios. Increasing water saturation of both layers produced low reflection-coefficient values that approached a minimum at 24% water saturation. At this point, the reflection coefficient reversed polarity and reached a maximum value of 0.11 value at 100% water saturation (fig. 8B). Single-stack reflection-coefficient values did not exceed the 0.10 threshold of Annan (1996) until water saturations exceeded 85%, higher than in the previous quartzose model. As mentioned previously, the lower sandstone layer would be expected to exhibit higher water saturation than the upper. If the model were altered so that the upper layer were at a constant water saturation of 10%, then single-stack reflection-coefficient values would exceed 0.10 only when water saturations in the lower layer were greater than 27%, when the lower layer contains mica (worksheet 5).

Example 2: Estuarine Sandstone Modeling

Incised valley-fill estuarine sandstones of the Tonganoxie Sandstone Member of the Upper Pennsylvanian Stranger Formation, northeast Kansas, representing medium-lower to fine-grained quartzose sandstone, siltstone, and shale lithologies were analyzed and described in Martinez, Beaty et al. (1998). Mineralogically, the samples consist primarily of quartz with varying amounts of disseminated and finely bedded argillaceous material (mainly illite clay). Core plugs measuring approximately 2.5 cm in diameter and 2.5 cm long were obtained from outcrop samples using a diamond core drill and diamond saw with tap water as coolant. Samples were oven dried and measured for helium porosity, hydraulic (air) permeability, and dry and partially water-saturated dielectric constant. Dielectric-constant values were measured on the dry and partially water-saturated cores and shale pieces over a frequency range of 750–1,500 MHz using the procedure described in Martinez and Byrnes (1999). On the dry samples, the average dielectric-constant values ranged from 6.9 for shales to 1.5 for high-porosity (38%) quartzose sandstone; on the samples with a water saturation of approximately 60%, the average values ranged from 15 to 6. Measurements on the samples after an extended period of exposure to the atmosphere, leading to a slight increase in water saturation by water adsorption, resulted in a significant increase in the bulk dielectric constant (fig. 9A). Knight and Endres (1990) noted a similar abrupt increase in dielectric constant (at very low water saturations in shaly sands) and related it to geometric and fluid-rock interaction effects on the pore surfaces. Once three or four monolayers of water are adsorbed on the rock surface, the influence of remaining increases in water saturation can be predicted closely using TP modeling.

Time-propagation modeling indicates that dielectric constant decreases with increasing air-filled porosity, increasing amount of quartz in the matrix, and decreasing water saturation. Figure 9A illustrates the relationship between dielectric constant and porosity for samples of varying water saturation. To account for fluid-rock electrochemical interaction due to increasing shaliness and increasing surface area with decreasing porosity, the dielectric constant for the air-dried (and not oven-dried) samples was assumed to represent the dry condition or baseline. This approach, also used by Knight and Endres (1990), accounts for geometric and fluid-rock electrochemical interaction effects on the wetted surface by incorporating them into the dielectric constant of the matrix. Once these effects are accounted for, the TP model

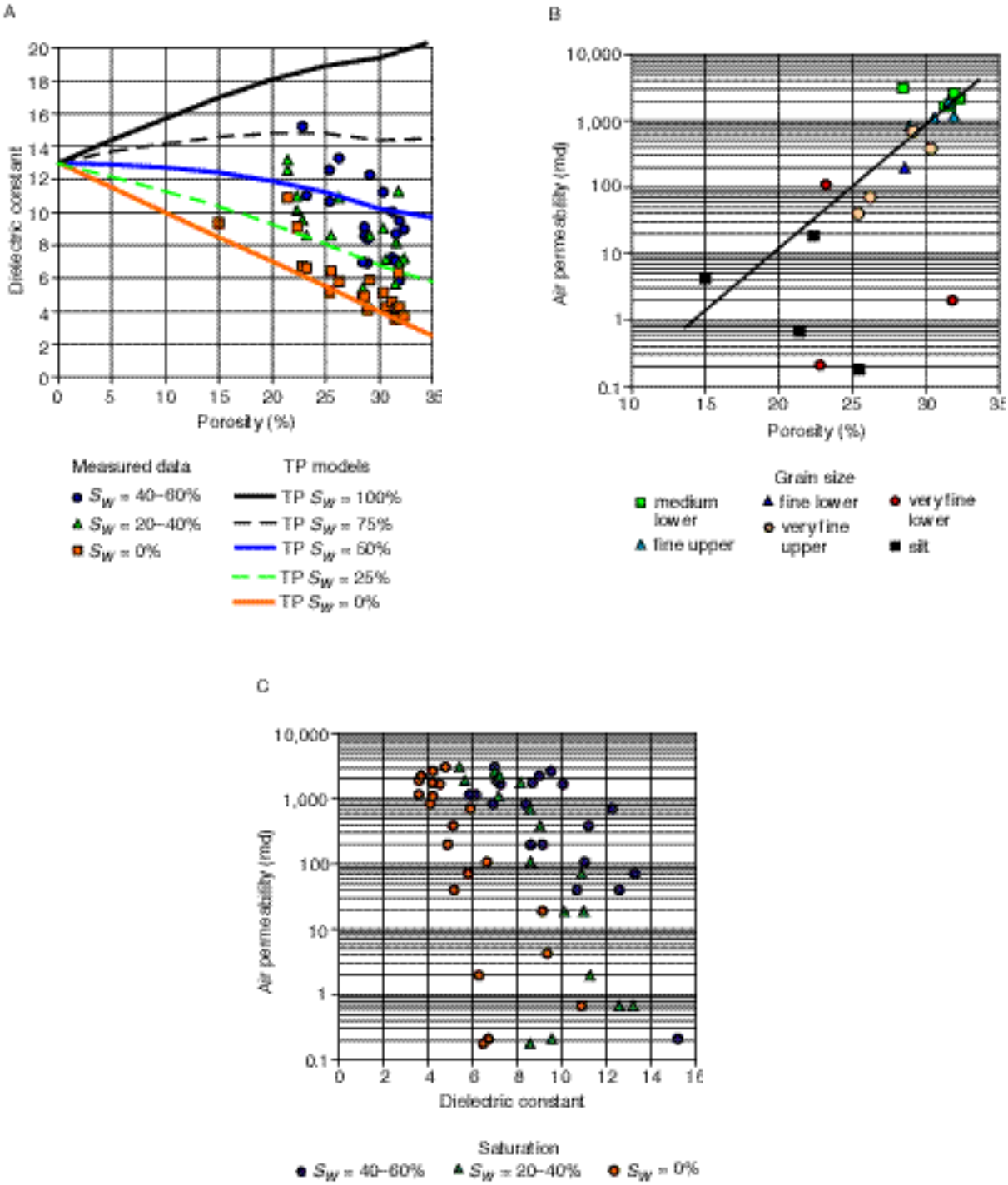

FIGURE 9. Results of laboratorymeasurements from Tonganoxie Sandstone estuarine sandstone, shaly sandstone, siltstone, and shale samples. (A) Measured dielectric constant versus helium porosity for water saturations of 0% (oven-dried), approximately 0% (air-dried), 20–40%, and 40–60%. The TP-model dielectric-constant curves for different water saturations (red line shows baseline conditions) are also shown. (B) Hydraulic (air) permeability versus helium porosity, with a log-linear correlation of $R^2 = 0.92$ (excluding siltstone samples). (C) Dielectric constant for air-dried samples versus hydraulic (air) permeability.

provides more accurate prediction of bulk dielectric constant for shaly sands.

Baseline dielectric constants for rock with increasing matrix dielectric constant and decreasing porosity, due to changing mineralogy, ranged from 4.4 (quartzose) at 35% porosity to 13.0 (shale-siltstone) at 0% porosity. Figure 9A shows dielectric-constant curves for four water saturations calculated using TP modeling from baseline conditions (yellow line). Measured dielectric-constant values exhibit a trend with porosity that is roughly consistent with TP

model-predicted values. Variance between TP model-predicted values and measured values may be attributed to difficulties in accurately measuring dielectric constants from coarse-grained samples, differences in mineralogy between the sample and the modeled matrix dielectric constant, and differences between actual sample water saturations and modeled curve values.

The Tonganoxie estuarine sandstones (excluding siltstones) exhibit a good log-linear correlation between hydraulic (air) permeability and porosity (R^2 = 0.92; fig. 9B). Based on the good correlations between hydraulic permeability and porosity and between baseline dielectric constant and porosity, an empirical log-linear correlation between hydraulic permeability and dielectric constant (fig. 9C) indicates that dielectric constant can be used to predict permeability.

Example 3: Limestone Modeling

Lime wacke-packstone, siltstone, chert, and limey shale lithologies of the Merriam Limestone Member of the Upper Pennsylvanian Lansing Group were collected from the study site of Martinez, Kruger et al. (1998). Mineralogically, the samples consisted primarily of calcite with varying amounts of chert (quartz) and disseminated argillaceous material (mainly quartz). Helium porosity, hydraulic (air) permeability, and dry and water-saturated dielectric constant were measured on the core plugs, using the same techniques used for the samples from the Tonganoxie Sandstone Member. Bulk dielectric-constant measurements were complicated by the heterogeneous nature of the rocks. Many samples exhibited lithologies with patchy bioturbated mudstones and packstones, each of which had a different dielectric constant. Bulk dielectric constants of these samples were obtained by averaging point dielectric-constant values weighted appropriately for the relative portions of each lithology in the total sample. In contrast to the Tonganoxie shaly sands, the air- and oven-dried carbonate samples had similar dielectric-constant values, which is consistent with their low clay content. In dry samples, average dielectric-constant values ranged from 7.9 for packstone (with low amounts, less than 5% of argillaceous material) to 3.1 for chert. Average dielectric-constant values in water-saturated samples ranged from 21.7 to 8.8.

Dielectric-constant values were predicted by TP modeling for rock with a calcite (ε_r = 8.0) and quartz (ε_r = 4.5) matrix and were simulated over the range of porosity values exhibited by the data (ϕ = 0% to 25%). The calculated values were plotted with the measured data (fig. 10A). Packstone samples that exhibited bulk dielectric-constant values less than the TP model-predicted values for a pure calcite (ε_r = 8.0) matrix contained varying amounts of quartz in the matrix in the form of increasing argillaceousness or chert. Incorporating matrix composition and porosity in the TP model-predicted values provided a better correlation with measured dielectric-constant values (standard error of prediction of 0.58) than the correlation with the calcite and quartz matrix trends evident in fig. 10A.

These carbonate rocks exhibited a good log-linear correlation between hydraulic (air) permeability and porosity (R^2 = 0.87; fig. 10B). However, the complexity of the relationship between dielectric constant and porosity, introduced by mineralogy (evident in fig. 10A) and sample heterogeneity, significantly weakens the correlation between dielectric constant and hydraulic (air) permeability (fig. 10C). Multivariate regression, using both dielectric constant and amount of quartz in the matrix, would improve the correlation, but not enough samples were studied for this analysis to be meaningful on this data set.

Discussion of Model Results

Comparison of the TP-modeled bulk dielectric constants with those measured on sandstone and limestone indicates that the TP-modeled values are reasonably well correlated with measured values. Both theoretical modeling (figs. 1 and 2) and measured data illustrate the significant influence of water saturation and porosity and the lesser influence of mineralogy on bulk dielectric constant and consequently on GPR response, including two-way travel time, reflection coefficient amplitude across interfaces of different materials, and vertical and horizontal imaging resolution.

The large increase in two-way travel-time (*TWT*) values with increasing water saturation (figs. 6–8) indicates that care must be taken when interpreting GPR data taken at the same site if water-saturation conditions change between surveys or differ across the site due to proximity to a water recharge or discharge area. For the sandstone scenarios shown in figs. 6–8, *TWT* increased rapidly with increasing saturation (fig. 11). Large travel-time changes induced by low water saturation differences may result in enough change in reflection-peak or trough-arrival times to cause mis-ties when interpreting data sets collected under different water saturation conditions. Similarly, it may result in misinterpretation of apparent bed dip if constant lateral saturations are assumed but are not present at a site.

Perhaps most important to understanding GPR images, and the limits of GPR imaging, is understanding reflection coefficients at interfaces between rocks exhibiting different bulk dielectric constants. Equations (3) and (4) provide the framework for analyzing reflection-coefficient differences that result from differences in bulk dielectric constant predicted by mixing models. It is evident from fig. 7 that the influence of porosity differences is more pronounced when water occupies the pores. Based on the scenario shown in fig. 7, for single-fold data in dry sandstone, porosity differences between beds must exceed approximately 35% to obtain a reflection coefficient greater than 0.1 (fig. 11). Such a great difference is unlikely except between high porosity sands and shales or siltstones. If 128-fold stacking is performed, then a

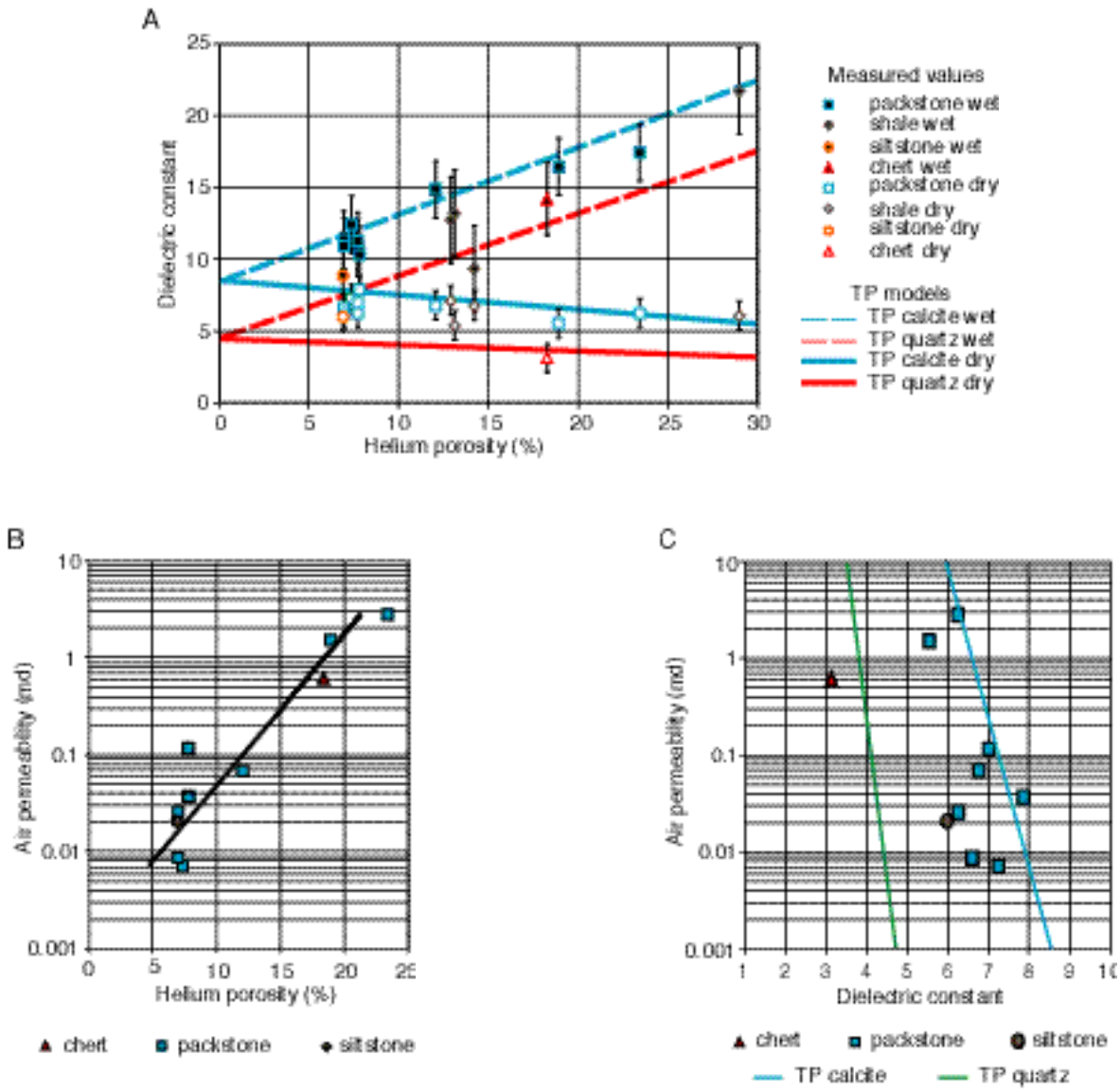

FIGURE 10. Results of laboratory measurements from carbonate samples collected at the Martinez, Kruger et al. (1998) study site, shown in conjunction with TP-model results for calcite (ε_r = 8.5) and quartz (ε_r = 4.5). (A) Dry and water-saturated dielectric constant versus helium porosity. (B) Hydraulic (air) permeability versus porosity, with a log-linear correlation of R^2 = 0.8743. (C) Dry and water-saturated dielectric constants versus hydraulic (air) permeability.

porosity difference of approximately 3 porosity percent can produce observable reflections. However, it requires an increase to approximately 1,024-fold stacking to lower the porosity difference threshold to approximately 1 porosity percent. As shown in figs. 6–8, the presence of water in the pores can cause large changes to the reflection coefficient, if water is in one layer and not the other. If, however, water is present in both layers, then increasing water saturation can be associated with an initial decrease in reflection coefficient, requiring greater stacking to maintain signal-to-noise ratios. Worksheet 5 (appendix A) allows calculation of TWT and RC for three layers of specified properties and can be used to investigate RC changes in response to layer properties.

Figure 12 illustrates the influence of variations in the matrix content on reflection coefficient, assuming no electrochemical interactions. The figure represents a two-layer model with constant porosity of 20% in both layers and with an upper quartzose sandstone layer overlying a lower mixed carbonate (ε_r = 8.5) and quartz (ε_r = 4.5) layer. When the quartz content increases to 100% in the lower layer, the reflection coefficient decreases to zero because the lower and upper layers become identical in matrix composition. When only mineralogy is changed, the amount of calcite in the matrix must be greater than 65% to produce a reflection coefficient greater than 0.10 in dry rocks for single-fold data. In water-saturated rocks, these mineralogic differences are so small compared to the

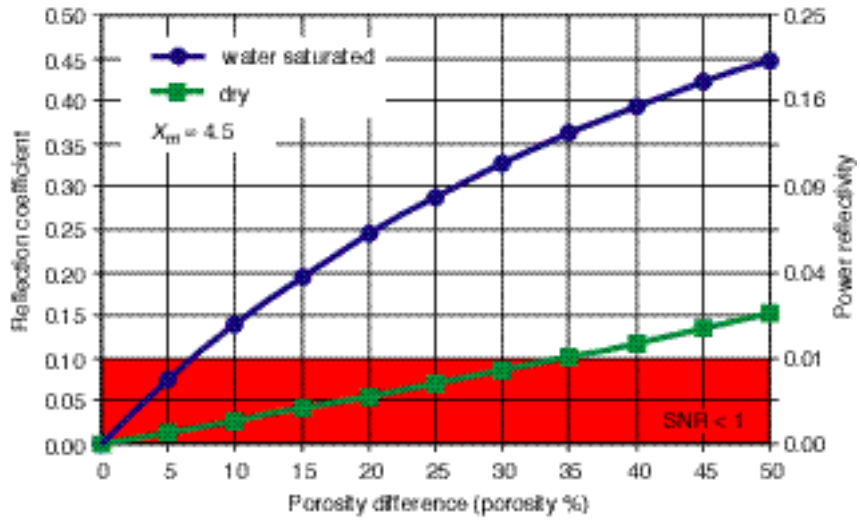

FIGURE 11. Calculated reflection coefficients for dry and water-saturated quartzose (ε_r = 4.5) models plotted against porosity differences ranging from 0% to 50%. The shaded area indicates power reflectivity values of less than 0.01, a conservative estimate of the threshold at which background noise may preclude recording of reflection information (i.e., SNR ≤ 1; Annan, 1996).

dielectric constant of the water in the pore space that reflection-coefficient values never exceed the threshold of 0.10. For 128-fold data, as little as 5% calcite in a dry quartz sandstone can produce an observable reflection and 15% calcite content will produce an observable reflection when both layers are water-saturated. In rocks, such as shaly sands, where geometric and fluid-rock electrochemical interactions may significantly increase the matrix dielectric constant, the influence of these effects must be accounted for by modifying model input parameters based on measurements from representative samples. These calculated reflection-coefficient values (fig. 12) show that 128-fold data are capable of imaging interfaces between beds with relatively small differences in mineralogy provided that water saturations are known.

Capillary-pressure differences are likely to result in low water saturations in high porosity, coarse-grained rocks and in higher water saturations in low porosity, fine-grained rocks and shales. While such differences might be expected to result in large reflection-coefficient values (as between sands and shales, for example), in fact, decreased porosity in finer-grained rocks results in less pore space available for water and a smaller bulk dielectric constant, even with the pores of the shale completely saturated. For example, in a shale that is 50% quartz (ε_r = 4.5) and 50% mica (ε_r = 6.5) and has 8% porosity that is water saturated (ε_r = 81), the bulk dielectric constant, calculated using the TP model, is only 8.2. At an interface with relatively dry (S_w < 20%) quartz sand with porosity between 0% and 50% (bulk ε_r ~ 4.5–5.7), single-fold reflection coefficients range from 0.10 to 0.15, equal to or only slightly above background noise (*RC* = 0.10). For carbonates interbedded with calcareous shales (bulk ε_r ~ 10.8), similar reflection-coefficient values are exhibited for similar ranges in porosity and water saturation.

Vertical imaging resolution can be calculated using worksheet 6 (appendix A), which utilizes Eq. (7). For rocks with a bulk dielectric constant of 2.5, vertical imaging resolution ranges from 0.2 m to 0.1 m at GPR frequencies of 200–400 MHz and decreases to 0.06–0.03 m in rocks with ε_r = 30. Thus, in rocks with low and high dielectric constants, GPR vertical resolution is capable of imaging fine-scale (less than 20 cm) bedding features. The long radii of GPR footprints for frequencies of 200–400 MHz in rocks with bulk dielectric constants ranging from 2.5 to 30 are approximately 1.7 m to 0.4 m, respectively, at 2-m depth (calculated using worksheet 7). These footprints indicate that small lateral changes in rock properties may not be precisely resolved. In addition, many GPR surveys are conducted using 125–450 Mhz antennas. Whereas this difference in frequency may significantly change vertical resolution, the footprint size at 2 m decreases by less than 20% from 125 MHz to 450 MHz. This suggests that some smaller-scale features in near-surface rocks and sediments are unresolvable using GPR.

Conclusions

Ground-penetrating radar is an increasingly popular geophysical imaging technique for geologic, environmental, and archeological studies. However, GPR results can easily be misinterpreted if the parameters controlling that response are not well understood. Dielectric-constant modeling provides a basis for better understanding the effects of mineralogy, porosity, and fluid saturation on bulk dielectric-constant values and, consequently, on GPR response. Based on correlation with measured sandstone and limestone samples, TP modeling provides reliable bulk dielectric-constant values, which can be used to understand GPR reflection coefficient signs and amplitudes,

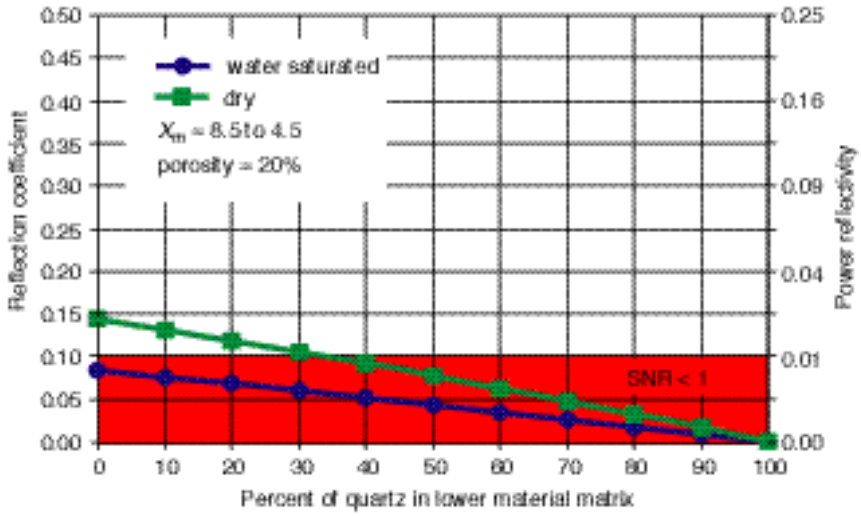

FIGURE 12. Calculated reflection coefficients for dry and water-saturated, two-layer models plotted against the percentage of quartz in the lower layer. The upper layer is 100% quartz with a 20% porosity, and the lower layer is calcite with variable amounts of quartz and a 20% porosity. The shaded area indicates power reflectivity values of less than 0.01, a conservative estimate of the threshold at which background noise may preclude recording of reflection information (i.e., SNR ≤ 1; Annan, 1996). The effect of mineralogy on reflection coefficients is less than that due to porosity (fig. 11).

two-way-travel times, vertical resolution, and the scale of GPR footprints.

Time-propagation modeling of the influence of porosity, mineralogy, and water saturation indicates that water saturation exerts a first-order influence on bulk dielectric constant and that mineralogy and porosity exert a second-order influence, though the relationship between these variables is highly interactive. Thus, water saturation is a variable that must be known to some degree for accurate GPR interpretation. Given that capillary properties, and thus water saturations, are likely to vary with lithofacies, modeling in this study indicates that higher water saturations may enhance GPR response. Conversely, overly dry subsurface conditions may eliminate any response. One could argue that some sites should be watered before performing a GPR survey or that optimal survey conditions may follow rainy periods. In addition, TP modeling for conditions at a site may provide information important to the design of the GPR survey.

Modeling performed in the study demonstrates that GPR response varies significantly with typical variations in rock and soil saturation, porosity, and mineralogy. Thus, interpretation of GPR data should either incorporate consideration of these variables and modeling or should be performed with caution. Conversely, modeling has shown that GPR response can be sensitive to subtle differences in rock properties and therefore can be a powerful tool for investigating subsurface properties. With inverse modeling—that is, using measured field GPR data and TP modeling—it may be possible to back-calculate the rock properties required to produce the observed GPR response. Further, if good correlations exist between porosity or dielectric constant and hydraulic permeability, as found for some rocks in this study, subsurface permeability may be predicted.

Given the theoretical sensitivity shown here of GPR response to the fundamental rock properties of porosity, water saturation, mineralogy, and hydraulic permeability, it is likely that refinement and further calibration of this type of modeling will improve and enhance the information obtained from GPR and potentially broaden its application. TP-modeled dielectric-constant values also can be used to populate geologic models used for waveform modeling.

Appendix A

An Excel workbook with interactive spreadsheets that use the formulas presented in the text is described in this appendix. This full workbook can be downloaded **(**http://www.kgs.ukans.edu/Current/2001/martinez/Appendix_A.xls**)** and used to determine many properties related to dielectric constant in geologic materials and to forward-model dielectric constant. These calculated values and models can in turn be used for modeling expected GPR response in field studies and aid in designing GPR surveys and interpreting GPR data. The downloadable workbook contains the worksheets listed below.

1) Dielectric Constants Worksheet

This worksheet contains a summary of the mineral and fluid dielectric constant data given in table 2.

2) TP Model—Porosity-Mineralogy Worksheet

This worksheet contains the TP-model equation, Eq. (1), for a three-layer example with fixed, user-defined

water saturations and variable matrix mineralogy and porosity (fig. 1). Each layer provides for a two-component matrix (e.g., quartz and mica) and two fluids filling the pore volume (e.g., air and water).

3) TP Model—Porosity-S_w Worksheet

This worksheet contains the Time-Propagation model equation, Eq. (1), for a three-layer example with a fixed, user-defined matrix mineralogy and variable porosity and water saturation (figs. 1 and 2). Each layer provides for a two-component matrix (e.g., quartz and mica) and two fluids filling the pore volume (e.g., air and water).

4) RC—Porosity-Mineralogy Worksheet

This worksheet allows calculation of reflection-coefficient values, Eq. (3), for models with variable porosity and mineralogy (figs. 11 and 12), allowing investigation of the sensitivity of GPR response to these variables. It also contains the formula for calculation of needed stacking parameters to achieve a reflection coefficient of 0.1 (fig. 3).

5) Modeled TWT and RC Worksheet

This worksheet calculates two-way travel-time and reflection coefficient for a three-layer problem with input of layer mineral and fluid properties, Eqs. (3) and (5).

6) Vertical Resolution Worksheet

This worksheet contains Eq. (7), used to calculate expected resolution (fig. 4). It also contains the summary of reported bulk dielectric-constant values for earth materials given in table 1.

7) Spatial Resolution Worksheet

This worksheet contains Eqs. (8) and (9), used to calculate expected spatial resolution (fig. 5).

References

Alharthi, A, and Jange, J., 1987, Soil saturation—Dielectric determination: Water Resources Research 23, p. 591–595.

Annan, A. P., 1996, Ground-penetrating Radar: Workshop Notes, Sensors and Software, Inc., Misissauga, Ontario, 106 p.

Annan, A. P., Cosway, S. W., and Redman, J. D., 1991, Water table detection with ground-penetrating radar: Society of Exploration Geophysicists, Annual Meeting, Extended Abstracts, v. 61, p. 494–496.

Baker, G. S., 1998, Applying AVO analysis to GPR data: Geophysical Research Letters 25, no. 3, p. 397–400.

Birchak, J. R., Gardner, C. G., Hipp, J. E., and Victor, J. M., 1974, High dielectric constant microwave probes for sensing soil moisture: Proceedings of the Institute of Electrical and Electronics Engineers, January 1974, v. 62, p. 93–98.

Botelho, M. A., Mufti, I. R., and Neto, V. P., 1998, Multishot prestack depth migration—An application on real wide-angle reflection and refraction GPR data: Society of Exploration Geophysicists, Annual Meeting, Extended Abstracts, v. 68, p. 1,393–1,396.

Daniels, D. J., 1996, Surface-penetrating radar—IEE Radar, Sonar, Navigation and Avionics Series 6: London, The Institue of Electrical Engineers, 320 p.

Davis, J. L., and Annan, A. P., 1989, Ground-penetrating radar for high-resolution mapping of soil and rock stratigraphy: Geophysical Prospecting 37, p. 531–551.

Dobson, M. C., Ulaby, F. T., Hallikainen, M. T., and El-Rayes, M. A., 1985, Microwave dielectric behavior of wet soil—II, Dielectric mixing models: Institute of Electrical and Electronics Engineers,Transactions on Geoscience and Remote Sensing, v. 23, p. 5–46.

Dolphin, L. T., Beatty, W. B., and Tanzi, J. D., 1978, Radar probing of Victorio Peak, New Mexico: Geophysics 43, no. 7, p. 1,441–1,448.

Keller, G. V., 1989, Electrical properties; *in*, Practical Handbook of Physical Properties of Rocks and Minerals, R. S. Carmichael, ed.: Boca Raton, FL, CRC Press, p. 359–428.

Knight, R., and Endres, A., 1990, A new concept in modeling the dielectric response of sandstones: defining a wetted rock and bulk water system; Geophysics 55, No. 5, 586–594.

Knoll, M. D., 1996, A petrophysical basis for ground-penetrating radar and very early time electromagnetics, electrical properties of sand-clay mixtures: unpublished Ph.D. dissertation, University of British Columbia, 316 p.

Knoll, M. D., and Clement, W. P., 1999, Vertical radar profiling to determine dielectric constant, water content, and porosity values at well locations; *in*, Proceedings of the Symposium on the Application of Geophysics to Engineering and Environmental Problems, March 14–18, 1999, Oakland, California, M. H. Powers, L. Cramer, and R. S. Bell, eds.: Englewood, Colorado, Environmental and Engineering Geophysical Society, p. 821.

Lange, J. N., 1983, Microwave properties of saturated reservoirs: Geophysics 48, p. 367–375.

Liner, C. L., and Liner, J. L., 1995, Ground penetrating radar—A near-face experience from Washington County, Arkansas: The Leading Edge, v. 14, no. 1, p. 17–21.

Lucius, J. E., Olhoeft, G. R., Hill, P. L., and Duke, S. K., 1989, Properties and hazards of 108 selected substances: U.S. Geological Survey, Open-file Report 89-491, 538 p.

Lichtenecker, K., and Rother, K., 1931, Die Herleitung des logarithmischen Mischungsgesetz es aus allgemeinen Prinzipien der stationären Strömung: Physikalische Zeitschrift, v. 32, p. 255–260.

Martinez, A., Beaty, D. S., Stiles, J., and Carr, T. R., 1998, Comparison of ground-penetrating radar reflectivity and rock properties in a sandstone-dominated incised valley-fill deposit; *in*, Proceedings of the 7th International Conference on Ground-Penetrating Radar, May 27–30, Lawrence, Kansas: University of Kansas Center for Research, Inc., p. 693–698.

Martinez, A., Kruger, J. M., and Franseen, E. K., 1998, Utility of using ground-penetrating radar in near-surface, high-resolution imaging of Lansing-Kansas City (Pennsylvanian) Limestone reservoir analogs: Current Research in Earth Sciences, Kansas Geological Survey, Bulletin 241, p. 43–59.

Martinez, A., and Byrnes, A., 1999, Dielectric probe procedures: Kansas Geological Survey, Open-file Report 99-1, 17 p.

McMechan, G. A., Loucks, R. G., Zeng, X., and Mescher, P., 1998, Ground-penetrating radar imaging of a collapsed paleocave system in the Ellenburger dolomite, central Texas: Journal of Applied Geophysics 39, p. 1–10.

Olhoeft, G. R., and Strangway, D. W., 1975, Electrical properties of the first 100 meters of the moon: Earth and Planetary Science Letters, v. 24, p. 394–404.

Olhoeft, G. R., 1989, Electrical properties of rocks; *in*, Physical Properties of Rocks and Minerals, Y. S. Touloukian, W. R. Judd, and R. F. Roy, eds.: New York, New York, Hemisphere Publishing Corporation, p. 257–329.

Powers, M. H., 1997, Modeling frequency-dependent GPR: The Leading Edge, v. 16, no. 11, p. 1,657–1,662.

Pratt, B. R., and Miall, A. D., 1993, Anatomy of a bioclastic grainstone megashoal (Middle Silurian, southern Ontario) revealed by ground-penetrating radar: Geology, v. 21, p. 223–226.

Reppert, P. M., Morgan, F. D., and Toksoz, M. N., 1999, Ground-penetrating radar and AVO; *in*, Proceedings of the Symposium on the Application of Geophysics to Engineering and Environmental Problems, March 14–18, 1999, Oakland, California, M. H. Powers, L. Cramer, R. S. Bell, eds.: Environmental and Engineering Geophysical Society, Englewood, Colorado, p. 593–600.

Roth, K., Schulin, R., Fluhler, H., and Attinger, W., 1990, Calibration of time domain reflectometry for water content measurement using a composite dielectric approach: Water Resources Research, v. 26, p. 2,267–2,273.

Schon, J. H., 1996, Physical Properties of Rocks—Fundamentals and Principles of Petrophysics (Seismic Exploration Series, no. 18): Tarrytown, New York, Pergamon Press, 583 p.

Sen, P. N., Scala, C., and Cohen, M. H., 1981, A self similar model for sedimentary rocks with application to the dielectric constant of fused glass beads: Geophysics 46, p. 1,302–1,311.

Topp, G. C., Davis, J. L., and Annan, A. P., 1980, Electromagnetic determination of soil water content—Measurement in coaxial transmission lines: Water Resources Research 16, p. 574–582.

Ulaby, F. T., Moore, R. K., and Fung, A. K., 1986, Microwave remote sensing, active and passive, Volume III—From theory to applications: Dedham, Massachusetts, Artech House, p. 2,017–2,119.

Ulaby, F. T., Bengal, T. H., Dobson, M. C., East, J. R., Garvin, J. B., and Evans, D. L., 1990, Microwave dielectric properties of dry rocks: Institute of Electrical and Electronics Engineers, Transactions on Geoscience and Remote Sensing, v. 28, no. 3, p. 325–336.

Ulriksen, C. P. F., 1982, Application of impulse radar to civil engineering: Unpublished Ph.D. thesis, Department of Engineering Geology, University of Technology, Lund, Sweden, 175 p.

Wang, J. R., 1980, The dielectric properties of soil-water mixtures at microwave frequencies: Radio Science, v. 15, p. 977–985.

Wang, J. R., and Schmugge, T. J., 1980, An empirical model for the complex dielectric permittivity of soils as a function of water content: IEEE Transactions Geosciences and Remote Sensing GE-18, p. 288–295.

Wharton, R. P., Hazen, G. A., Rau, R. N., and Best, D. L., 1980, Electromagnetic propagation logging—Advances in technique and interpretation: Society of Petroleum Engineers, Paper 9267, 12 p.

Yilmaz, O., and Doherty, S. M., 1987, Seismic Data Processing—Investigations in Geophysics, no. 2: Tulsa, Oklahoma, Society of Exploration Geophysicists, 536 p.